Controlled Aerodynamic Loads on a Slender Axisymmetric Body at High Incidence

Edward Lee [1], You Huang [2], Bojan Vukasinovic [3], and Ari Glezer [4]
Woodruff School of Mechanical Engineering,
Georgia Institute of Technology, Atlanta, GA 30332-0405

Abstract

The flow over an inclined slender axisymmetric cylinder (L/D = 11) with an ogive forebody is investigated experimentally at high angles of attack up to α = 65°. Of particular interest is the evolution and control of net side forces that are associated with asymmetries of the forebody vortices. It is shown that the interactions of the forebody vortices with the near-wake vortices of the cylinder leads to the formation of a vertical stack of counter-rotating streamwise vortices whose order depends on the dominant asymmetry of the forebody vortex pair. Synthetic jet actuation applied at the juncture of the forebody leads reversal of the order of the vortex stack in the wake and consequently alters the net side force. The present investigations also demonstrated that unsteady coupling between the cylindrical body and its near wake can lead to strong yaw-roll instabilities. The manipulation of the body vortex system and the side force by flow control actuation can be used for bi-directional control of the body's trajectory and suppress this instability.

I. Background

Investigations of the aerodynamic characteristics of axisymmetric slender bodies at moderate and high incidence angles have been largely motivated by the flight dynamics of missiles, munitions, and fighter aircraft. These flight platforms encounter complex, unsteady aerodynamic loads that are usually far more significant at higher angles of attack and are associated with the appearance and evolution of trains of spatially and temporally varying vortical structures over the body and in its near wake. The earlier studies showed that these vortical structures are spearheaded by the formation and asymmetries of counter-rotating vortex pairs near the upstream end of the forebody. The dynamics and asymmetries of these forebody vortices and their interactions with vorticity concentrations within the oblique shear layers that bound each side of the near wake along the main cylindrical body and its aft segment can contribute to strong unsteady side- and cross-stream forces and yawing and pitching moments that may be used for attitude control.

---

[1] Graduate Research Assistant, AIAA Member.
[2] Graduate Research Assistant, AIAA Member.
[3] Research Engineer, AIAA Member.
[4] Professor, AIAA Fellow.

In one of the early investigations of the forebody vortices, Nelson and Fleeman (1975) attributed the induced changes in side force and yawing moment on the cylinder to asymmetric shedding of vortices from its leeward side. Yanta and Wardlaw (1977) noted the asymmetry of the forebody vortices and flow at high inclination angles can be caused by minor variations of the nominally axisymmetric forebody, and in a subsequent investigation (Yanta and Wardlaw, 1981) attributed the side force that occurs when one of the forebody vortices detaches from the body to the opposite sense vortex that remains attached. Subsequently, these authors found that the asymmetric vortex pattern ($\alpha = 45°$) is formed as a result of secondary vortices that develop adjacent to the primary forebody vortices, causing one of the primary vortices to become detached from the surface (Yanta and Wardlaw 1982).

Based on simulations and flow visualization studies of the forebody vortex flow over a range of angles of inclination in various studies (e.g., Wu et al., 1986, Ward and Katz 1989a, 1989b, 1989c, Zilliac et al. 1991, and Deng et al. 2003), the topology of the forebody vortices over a range of inclination angles can be divided into three primary regimes. These regimes include: symmetric vortices that are mostly jointly located adjacent to the surface of the cylinder or become jointly detached from the surface ($\alpha < 30^o$), asymmetric vortices where one of the counter-rotating vortices become detached first, leading to mutual roll ($30 < \alpha < 60^o$) and to significant side force and yawing moment, and unsteady wake-like flow when the vortices couple to the oblique and Kármán shedding off the cylinder section ($60 < \alpha < 90^o$).

At high angles of attack, simulations of asymmetric vortex shedding induced by a geometric perturbation on one side of the forebody of a slender ogive-cylinder ($\alpha = 70°$) by Ma and Liu (2014) showed that the wake of the main cylinder can be roughly divided into two main streamwise domains. This is consistent with the observations of Thomson and Morrison (1971), where the upstream (5-7D long) domain comprises of a quasi-steady multi-vortex structure of the forebody vortex system, and the downstream domain is characterized by Karman vortex shedding. Ma and Liu (2014) reported a dominant wake frequency associated with each of the forebody and Kármán vortex shedding domains and noted that as the incidence increases, the upstream domain diminishes, as it can be expected. It is noteworthy that the simulations of Ma and Liu (2014) reveal interactions of the forebody vortices with streamwise vortices that form within the oblique shear layers on each side of the cylinder's near wake.

In an effort to mitigate asymmetric vortex formation and the associated increase in side forces and yawing moments, the utility of movable and/or deployable mechanical protrusions for reduction in aerodynamic side forces and moments has been investigated. Rao et al. (1987) tested deployable strakes on an isolated forebody ($L/D \approx 5$; $\alpha = 50°$) and reported large changes in the side forces with the strakes azimuthal angle that were associated with the formation of a 'strake vortex' that remained close to the forebody, or a larger-scale detached 'spoiler vortex'. Leu et al. (2005) utilized an array of inflatable micro-balloon actuators fixed to the surface of a conical forebody ($L/D = 5$) to induce the formation of asymmetric vortices and side forces of a desired direction. Stucke (2006) manipulated the forces, pitch and yaw moments, and roll angle of an inclined axisymmetric body ($L/D = 4$, $\alpha = 50°$) using spoilers and strakes near the leading edge. More recently, Mahadevan et al. (2018) triggered and managed the asymmetry of forebody vortices using boundary layer scale hemispherical protrusions on a highly polished conical forebody.

A number of investigations employed fluidic actuation (steady and unsteady blowing and suction) and limited plasma actuation near the tip of inclined forebodies to manipulate the shedding of the vortices from the leeward surface and thereby effect changes in the side forces and yawing moments. Steady jets have been used over a range of subsonic and transonic speeds and momentum coefficients (e.g. Almosnino and Rom, 1981, conical forebody, $L/D = 6$, $\alpha = 35° - 55°$, $C_\mu < 0.002$, and Skow et al., 1982, ogive forebody, $L/D = 3.5$, $\alpha = 35° - 55°$). Unsteady actuation using a linear array of synthetic jets along the leeward stagnation line of a conical forebody was used by Williams et al. (1989) and Williams and Papazian (1991) to form 'pneumatic' splitter plate and effect flow symmetry at $\alpha = 55°$. Similarly, Kalyankar et al. (2018) used unsteady sweeping jets on the side of an inclined cylinder ($L/D = 9$, $\alpha = 60°$) to alter the separation line on the surface and generate yaw moment as large as $\Delta C_{LN} \sim 0.8$ with $C_\mu = 2.7\%$. The "phantom yaw" effects associated with asymmetric vortex shedding over a pitching axisymmetric body ($L/D = 20$) were characterized in the recent simulations of Schnepf and Schülein (2018), who used steady blowing from a slot along the side of the body to mimic an 'aerostrake' and to mitigate asymmetric vortex shedding and reduce the aerodynamic side force by 25%. In a noteworthy approach, Sato et al. (2016) were able to reduce the side force and yawing moment on a cone-body ($L/D = 5.7$, $\alpha < 90°$) by up to 50% by using autonomous bleed driven through internal passages within a forebody cone by the external pressure differences. Plasma actuation was used by Fagley et al. (2012) to manipulate the asymmetric aerodynamic side force on an inclined forebody (Kármán ogive, $L/D = 3.5$, $40° < \alpha < 60$) by up to $\Delta C_y = \pm 1$. Considering the effectiveness of active actuation, a number of investigations have demonstrated closed-loop feedback control of the aerodynamic side forces induced by the forebody vortices. For example, the methodology of Porter et al. (2014) was recently adopted by Seidel et al. (2018) in a simulated closed loop feedback controller which could effect specified side forces.

The present investigation explores prescribed modification of the global unsteady aerodynamic loads on a slender axisymmetric body at high incidence by exploiting the coupled body-wake instabilities using aerodynamic flow control approaches. These investigations build on earlier findings of the effects of fluidic actuation on the aerodynamic loads on stationary and moving axisymmetric bluff bodies at low incidence (cf., Lambert et al., 2018). Although the most prior work considered the direct control of the forebody vortex pair by placing the flow control elements in the vicinity of their origin, the present effort focuses rather on the direct control of the coupled wake, which importance rises to the forefront with increasing incidence. Therefore, the present flow control approach affects the dominant streamwise vortices, and consequently the aerodynamic loads, in an indirect fashion.

II. Experimental Setup and Procedures

The present experimental investigation is concerned with the flow dynamics over a slender axisymmetric cylinder model ($L/D = 11$, $D = 40$ mm, $Re_D = 7.9 \cdot 10^4$), including the tangent ogive forebody of the length $l/D = 2$. As the prior studies indicated that the ogive body geometry generally induces more prominent side forces when compared to the conical forebodies (e.g., Chapman et al, 1976), the ogive geometry is utilized in the current investigation. The investigations are focused on control of autonomously-formed forebody vortices over a range of angles of inclination ($25° < \alpha < 65°$), while the wind tunnel was operated with uniform wind speed of $U_o = 30$ m/s, while the emphasis is placed on the high angle range $45° < \alpha < 65°$.

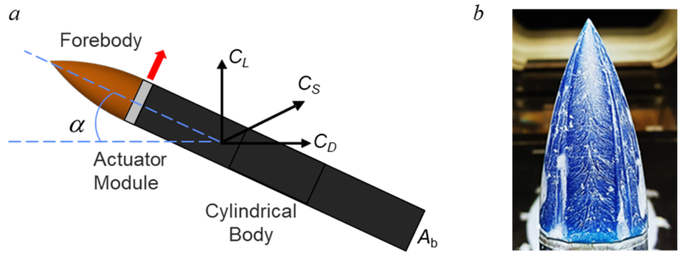

Figure 1. *Axisymmetric slender model (L/D = 11) with an ogive forebody having an integrated flow control module (a) and surface oil-flow visualization of the forebody vortices at an angle of attack α = 60° (l/D =2).*

The axisymmetric body is comprised of three major modules: the ogive forebody, synthetic jet actuator module, and the central cylindrical body, as illustrated in Figure 1a. Both the forebody and the jet module are designed such that can be rotated by the full azimuthal period. The azimuthal orientation of the forebody ϕ and the jet θ are referenced to the top vertical point, with the angles increasing clockwise, in the upstream view. The jet module incorporates a single azimuthal orifice measuring 0.6 × 15.7 mm, imparting the jet momentum coefficient C_μ while issuing normal to the surface at the frequency of about 2.3 kHz. To illustrate the forebody vortices that the control jet is designed to affect, the forebody vortex pair is visualized over the default l/D = 2 ogive forebody at the angle of attack α = 60°. For that purpose, a mixture of a titanium-oxide paint and the linseed oil is applied over the forebody, where its ratio is iteratively adjusted such that the oil mixture does not shear before the operating flow condition is attained. After the test section speed reached U_o = 30 m/s, the oil is sheared for about 20 minutes, and the resulting flow pattern is shown in Figure 6b in an upstream view from above. The two vortical traces are clearly seen in the image, forming off the forebody tip and evolving along the forebody surface. The strong traces along each line where the vortex lifts the flow away from the surface indicates that these vortices remain in the proximity of the surface over the full forebody extent.

The axisymmetric model is wire-supported in an open-return wind tunnel (test section measuring 91 cm on the side) by a dynamic 6-DOF eight-wire (1.2 mm dia.) traversing mechanism described in detail by Lambert et al. (2016). Each support wire is controlled by an independent servo motor, with an in-line load cell, and electrical connection for the flow control actuators is provided by thin wires weaved along the back four support wires while the support wires provide electrical ground. The forces and moments on the model are calculated from the measured wire tensions projected onto the model (the resultant aerodynamic loads on the model are calculated relative to the loads in the absence of cross flow, and accounting for wire drag). The attitude of the model is commanded by a *Matlab Simulink* controller, which feedback utilizes inputs from *VICON* motion-capture camera system at an update rate of 500 Hz. Besides providing the feedback signal, the six-camera motion capture system resolves the spatial and temporal position of the model at any instant in time. In an alternate configuration, the feedback loop can be disconnected and the model 'locked' in the desired attitude. Either configuration is utilized, depending on the objectives of the studies. The information regarding the model position/orientation is used to extract the wire orientation and accurately decompose the forces measured on each load cell into x, y, and z components in real time. In addition to the measurement of the aerodynamic loads, a stereo

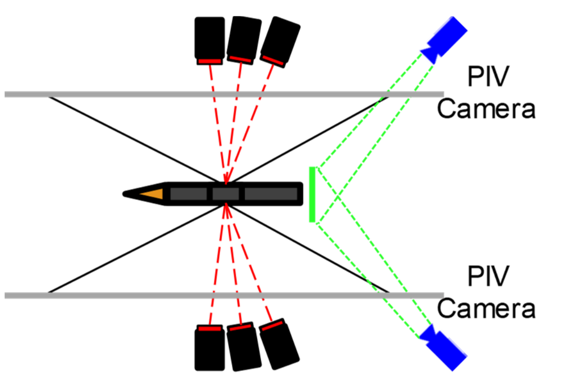

Figure 2. *Schematics of the top view of the supported model illustrating the stereo PIV wake measurements and positioning of the Vicon cameras for orientation tracking of the model.*

PIV (SPIV) system is used to characterize the model's wake dynamics using two CCD cameras that are each placed at an angle of 20° relative to an image plane normal to the oncoming flow at x/D= 2 – 9 from the tip of the model. Schematics in Figure 2 illustrates orientations of the two PIV and six motion-capture cameras that are distributed evenly on both sides of the test section.

In contrast to many of the prior investigations of fluidic control for affecting the symmetry of the forebody vortices, in the present investigations the upstream actuation jets were deliberately placed well downstream of the forebody tip, just downstream from the termination of the forebody, as illustrated in Figure 1a. The objective was to test whether the evolution of the flow dominant vortices would be susceptible to a rather indirect control of the coupled wake, instead of controlling the initial vortex formation at the forebody tip. For the control purpose, a single synthetic jet actuator (orifice measuring 0.6 × 15.7 mm) is integrated at the juncture between the forebody and the cylinder. The jet's azimuthal orientation θ is adjustable independently of the forebody azimuthal orientation ϕ.

III. The Base Flow

Initially, the aerodynamic loads on the cylindrical model were characterized in the absence of actuation over a range of inclination angles ($25° < \alpha < 65°$, $Re_D = 7.9 \cdot 10^4$) using the three ogive forebodies of l/D = 1, 2, and 3. The inclination angle of each model was increased monotonically from the same base angle to avoid hysteresis effects. In order to enable meaningful comparison between the models with the different ogive forebodies, the variation of the force coefficients C_D, C_L, and C_S were computed based on the model's planform area (including the forebody). Hoerner and Borst (1985) characterized the lift and drag on an inclined cylinder in the absence of a forebody. These authors noted that at low inclination ($\alpha \leq 15°$), the flow over the cylinder is predominantly oriented along its axis and it may be thought of as low-aspect-ratio wing with a pair of counterrotating "tip" vortices that form over the suction surface resulting in lift-induced drag. At higher angles of attack, the flow from the windward to the leeward face of the cylinder separates on its leeward face and generates a normal force on the body whose respective cross-stream and streamwise projections are the lift and drag. Both lift and drag forces are small for $\alpha \leq 15°$, and as α increases, the drag increases monotonically and reaches a maximum at $\alpha = 90°$, while the lift has a local maximum (around 55°), and then decreases monotonically and vanishes $\alpha = 90°$.

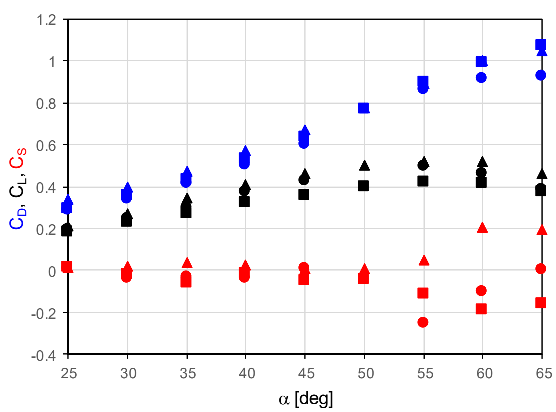

Figure 3. *Force coefficients C_D, C_L, and C_S with angle of attack α for the slender axisymmetric body ogive nose ratio l/D = 1 (square), 2 (triangle), and 3 (circle).*

On the present model, as seen in Figure 3, the drag increases monotonically over the entire range of α while the rate of increase of the lift begins to diminish for $\alpha > 35°$ ostensibly as the forebody vortices begin to lift off the cylinder and the flow from the windward separates on its leeward surface. Similar to the observations of Hoerner and Borst (1985), while the drag force continues to increase monotonically, the lift force has a maximum around $\alpha = 55°$, and then decreases at higher angles of incidence. While the drag coefficients for the three ogive forebodies are nearly identical through $\alpha \sim 60°$ the drag coefficient of the $l/D = 3$ ogive is lower at higher α and appears to reach a local maximum that is lower than the corresponding drag coefficients of the $l/D = 1$ and 2 ogives. However, the corresponding peak lift coefficients of the $l/D = 1$ ogive is lower than the coefficients of the other ogives. It is apparent that these changes are associated the changes in the side forces that remain nominally symmetric about the cylinder's vertical (y-z) plane of symmetry up to $\alpha \sim 50°$. According to earlier work (e.g., Keener and Chapman, 1974), the onset of the vortex asymmetry approximately scales with the forebody tip angle, which is 58° for the present model. As is evident from the variations of the side force coefficients, the onset of forebody vortex asymmetry which is affected by small variations in the ogive surfaces, varies between the different forebody models, and also affects both the lift and drag forces. For the remainder of the current study, the forebody is fixed at $l/D = 2$. In addition, it is observed during the pitch sweeps that the model, once in the non-zero side force domain, can undergo unstable motion, which is further addressed in Section V.

To gain a better understanding of the base flow features at high angles of attack, preliminary sPIV measurements are taken at three streamwise positions, measured from the forebody tip, $x/D = 2$, 5, and 9 while the body is oriented at $\alpha = 60°$. These locations are selected such to characterize the flow state just downstream from the location of the control jet, far over the body, and finally off the body, in the wake. Due to the wake spreading, the measurement resolution is adjusted with the downstream distance, such to capture the wake extent. For the same reason, measurements on the wake are taken over two measurement planes that are merged into a single composite flow field. The resulting captured flow field is shown in Figure 4, illustrating the dominant vortical composition of the flow. As it could be expected, the initial vortex pair, formed at the forebody, lifts off the surface shortly downstream from the forebody, due to the high incidence. Although still at the surface at $x/D = 2$, this pair evolves into a highly asymmetric pair at $x/D = 5$, where the CW vortex remains closer to the body, while the CCW vortex, rotated in pair with the CW one, moves away and nearly atop its CW pair. This relative orientation remains preserved into the wake at $x/D = 9$. Once the initial vortex pairs is peeled off, the successive folding of the flow over the cylindrical body results in the secondary vortex pair formation, which is just barely captured at the bottom end of the measurement plane at $x/D = 5$, and fully seen at x/D =9 underneath the primary vortex pair, and assuming a nearly identical relative orientation between the CW and CCW vortices. Besides these tow pairs of streamwise vortices, additional vortical concentrations are seen in the wake, as it is expected that the shear layers of the flow separating of the cylinder body partially contribute to the streamwise vortical components. Besides, each vortex can induce a neighboring lesser vortical motion of the opposite sense, which is likely manifested just below the lowest CW vortex at $x/D = 9$.

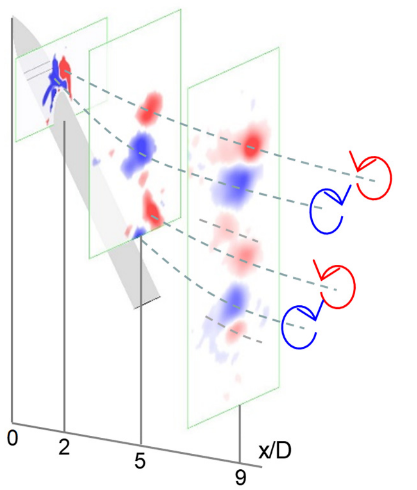

Figure 4. *Illustration of the base flow composition by the sPIV-measured flow fields at x/D = 2, 5, and 9, at* $\alpha = 60°$ *and* $Re_D = 7.9 \cdot 10^4$ *(l/D = 2, L/D = 11).*

The uneven liftoff of the vortex pair and its subsequent tilt about the common axis signalizes disruption in the side force balance and induces a net non-zero side force. Such a liftoff of one of the forebody vortices from the surface was documented in detail in a number of earlier studies (e.g., Lamont and Kennaugh, 1989, DeSpirito 2017, Mahadevan et al. 2018). Lamont and Kennaugh (1989) showed a nearly periodic switching in the direction of the side force as the forebody is rotated azimuthally about the axis of the cylinder over a range of incidence angles, which reflects the switching vortex asymmetry in the flow. As shown by Mahadeven et al. (2018) even fine polishing of the forebody surface was insufficient to fully suppress the vortex asymmetry and the direction switch of the induced side force. It should be noted that this sensitivity of the forebody vortices to small perturbations indicates their potential receptivity to flow control actuation as well.

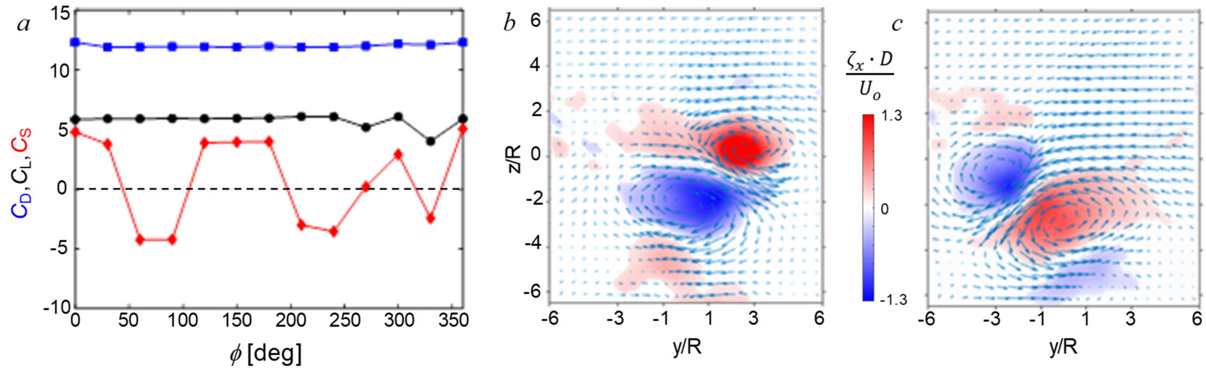

***Figure 5.** Force coefficients C_D (■), C_L (●), and C_S (♦) with the forebody azimuthal orientation ϕ (a), and the two spanwise mean velocity fields, measured at x/D = 9, with overlaid contour plots of the streamwise vorticity component at ϕ = 90° (b) and 180° (c) for the model at α = 60° (Re_D = 7.9·10^4).*

The asymmetry in the evolution of the forebody vortices and the resulting side forces is investigated at α = 60° (Re_D = 7.9·10^4) over a full azimuthal rotation of the l/D = 2 forebody. The resulting drag, lift, and side force coefficients (each normalized by the cylinder's cross sectional area A_b) are shown in Figure 5a. In concert with the earlier investigations, the side force exhibits azimuthally-periodic switching. However, $C_S > 0$ for most of the azimuthal orientations 100º < ϕ < 220º, 275º < ϕ < 50º and switches direction $C_S < 0$ only within narrow azimuthal domain centered about ϕ = 70º and 220º. One notable exception is a sudden drop of the side force at ϕ = 330°, which is caused by the body undergoing instability for that particular forebody orientation. It is interesting to note that the induced side force does not change its direction when the forebody is rotated at 180º relative to some given azimuthal position (i.e., C_S > 0 or < 0 at both domains although the nominal magnitudes of the opposite side forces are not necessarily of the same). That the sense of the side forces does not change when the forebody is rotated at 180º indicates that the flow asymmetry is likely not brought about by a random surface imperfection, because a strong periodic behavior of the present data (and a number of the earlier studies) suggest that the origin of such behavior is likely in the regular geometry deviation with a preferential axis. The most obvious source of such deviation would be an imperfect tip of the forebody, particularly since many investigations indicated extreme flow sensitivity to small geometrical perturbations at the forebody tip. Examination of the tip of the current forebody model indicated small oval deviation from the perfectly circular termination of the tip, and it is argued that such an oval shape with the dominant axis would be sufficient to induce preferential vortex asymmetry, depending on the dominant axis azimuthal orientation. Moreover, as the forebody is rotated by 180°, the oval orientation would assume the same orientation of its dominant axis, which would explain periodicity is the side force formation. As the oval manufacturing perturbation is not perfect, this would also explain that asymmetry in the magnitudes of the excursions and the disparity in their azimuthal extents are associated with the randomness of this deviation. It is remarkable that for fixed angles of incidence and yaw the lift and the drag are nearly invariant with ϕ even though the side force undergoes significant variations which are associated with topological changes in the trajectories of the streamwise forebody vortices. This indicates that once the vortices separate and migrate off the cylindrical body, their effects on the lift and drag diminish.

The changes in the topology of the vortex pair associated with the changes in the direction and magnitude of the side force in Figure 5a is illustrated in color raster plots of the time-averaged streamwise vorticity superposed with vectors of the cross-stream velocity field captured using stereo PIV within the domain $-6 < y/R < 6$, $-6.5 < z/R < 6.5$ ($x/D = 9$) for $\phi = 90°$ and 180° (Figure 5b and c, respectively). The data in each of Figures 5b and c show a dominant pair of counter-rotating streamwise vortices where the CW vortices in this view are associated with the rollup at the left side of the forebody (in this upstream view), along with additional, weaker streamwise vortices that would be shed within the cylinder's wake (cf. the simulations of DeSpirito 2017). As is evident from the vorticity concentrations, the major axis of the dominant vortex pair (i.e., the axis centered between the vortices, nominally normal to a line through the centers of their cores and pointing in the direction of the induced flow) in Figure 5b is *rotated* by 128° in Figure 5c (from 26° to 154°). As can be seen from Figure 5a, the directions of the major axes are asymmetric (i.e., the major axes in Figures 5b and c are pointing to the right and the left, respectively) and commensurate with the changes in the directions of the side forces namely $C_S < 0$ at $\phi = 90°$ and $C_S > 0$ at $\phi = 180°$. It is also noteworthy that the change in the directions of the major axes of the primary vortex pair is also accompanied by changes in the sense of the accompanying streamwise vortical traces that are captured within the field of view, ostensibly by reversal of the induced cross flow by the dominant vortex pair.

IV. Active Flow Control of Aerodynamic Loads

An initial assessment of the flow control effectiveness by a synthetic jet (Section III) is done by investigation of its performance with respect to its azimuthal orientation for a given flow control parameter C_μ, and for the fixed azimuthal orientation over a range of the control C_μs.

As the analysis of Figure 5 indicated, representatives for the two characteristic side force states $C_S < 0$ ($\phi = 90°$) and $C_S > 0$ ($\phi = 180°$) are sufficient to assess the effectiveness of the flow control. For brevity, only the $\phi = 90°$ case is presented here. As the base flow exerts a negative side force on the body in this case ($\alpha = 60°$, Figure 5a), the flow control that would counter such a force is sought within the $0 < \theta < 180$ azimuthal jet orientations. Having the forebody azimuthal orientation fixed, the synthetic jet is successively rotated within this range and the corresponding forces and angular orientations measured with the jet being active and inactive. The resulting data are shown in Figure 6 in terms of the realized force coefficients and angular orientations. As seen in Figures 6a,c,e, there is an azimuthal range of the flow control effectiveness, inducing over $\Delta C_S = 4$, while virtually no changes are recorded in C_D and C_L. It should be noted that the flow control completely counters the base flow side force, restoring the near-zero

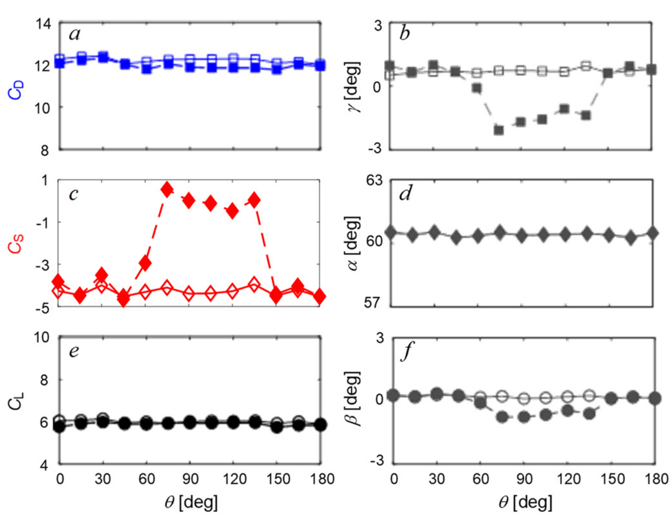

Figure 6. *Force coefficients C_D (a), C_S (c) and C_L (e) and the roll (b), pitch (d), and yaw (f) with the jet azimuthal orientation θ at $\alpha = 60°$.*

net force within 75 < θ < 135 . Along with the effect on the side force, the flow control effects changes on the body attitude, as displacements in both yaw and roll are measured. It should be noted, though, that the split in displacement in yaw and roll is due to the lab-fixed coordinate system. In the body-oriented coordinate system, most displacement would in its own yaw. Although not shown, the analogous test for the forebody orientation $\phi = 180°$ results in the flow control effective range within about mirror-image range of the jet azimuthal angles θ. Therefore, for the remainder of this study, the representative flow control jet orientation $\theta = 90°$ is selected for base flow negative side force ($C_S < 0$) and $\theta = 180°$ for the base flow positive force ($C_S > 0$).

Once the most effective azimuthal flow control orientations are pre-set, the next step concerns the sensitivity of such preferential azimuthal distance to the full range of the absolute forebody rotation. To test this, the jet orientation of $\theta = 90°$ is paired with the forebody orientation $\phi = 60°$ (see Figure 6), and then the forebody and the actuator azimuths are jointly reoriented back to zero orientation for the forebody. After that, both the actuator and the forebody are incremented jointly across the full span of the azimuthal angles, and the jet effectiveness is tested, keeping in mind that for any forebody orientation ϕ, the jet orientation $\theta = \phi + 30°$. By simultaneous rotation of both the forebody and the jet, the jet relative distance to the dominant axis of the forebody tip is maintained, while the tip disturbance imposes its full-rotation effect on the side force. The resulting changes in all the three force coefficients are shown in Figure 7. As it was the case in the fixed jet orientation, no significant effect is detected for the drag and lift forces. Initial incremental effect of the side force, as the forebody orientation assumes $\phi = 60°$ indicates the maximum jet effectiveness, as the jet itself is at $\theta = 90°$. It is seen that even beyond this orientation, the jet imparts nearly as strong effect as both the forebody and the jet are rotated for another 30° increment. At the following increment, it is interesting to note that significant effect is achieved, but of the opposite sign. By examining the corresponding base flow force at this orientation $\phi = 120°$ (Figure 5a), it is seen that the base flow force already switched its sign at this orientation, but the flow control jet, although located at $\theta = 150°$ is still capable of countering this now altered vortex asymmetry that brought about the change is sign of the base side force. As the jet and the forebody continue to advance azimuthally, small further changes are measured until the forebody orientation reaches $\phi = 240°$, and thereafter there is practically no jet effect. This is particularly interesting as a strong negative side force is generated at $\phi = 220° – 250°$ in the base flow (Figure 5a). The reason for the jet ineffectiveness for these orientations is in the fact that the base flow asymmetry is of the same sense for both $\phi = 90°$ and 240°. As shown in Figure 9a, the jet counters these asymmetries when oriented at $\theta = 90°$. However, in the present test, the jet is oriented exactly on the opposite side of the body and hence ineffective in countering the flow asymmetry at $\phi = 220° - 250°$, i.e., the jet is oriented on the same side with the body orientation. This study indicates that the flow control is clearly sensitive to the particular (albeit unknown) surface disturbance orientation, but that there is still an azimuthal range of the jet orientation that is sufficient to impart significant changes in the side force, predominantly by countering the naturally induced side force.

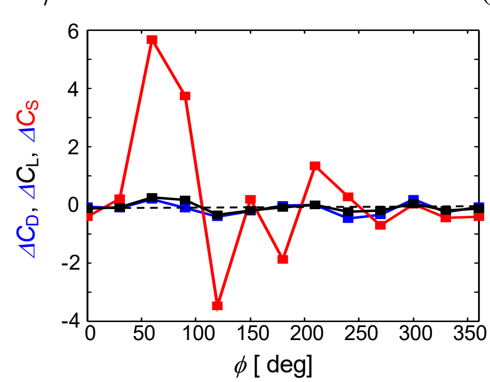

Figure 7. *Incremental change in the force coefficients C_D (■), C_L (■), and C_S (■) by the synthetic jet actuation with the forebody azimuthal orientation ϕ while the jet orientation is maintained at $\theta = \phi + 30°$.*

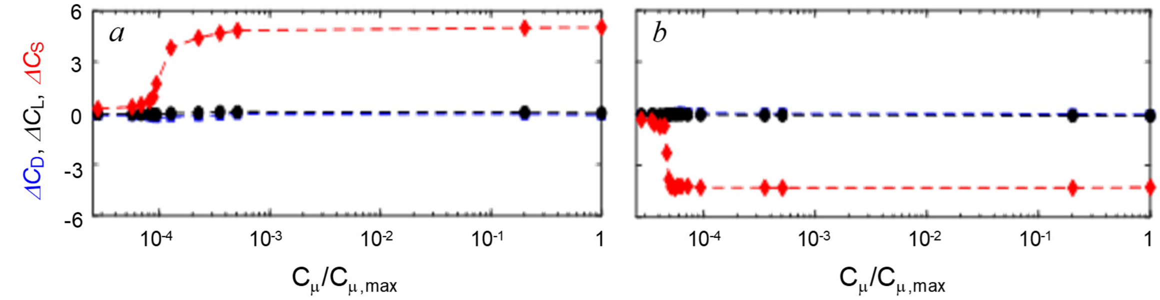

Figure 8. *Force coefficient change ΔC_D, ΔC_L, and ΔC_S with the control jet for the forebody and jet orientations (ϕ,θ)= (60°, 90°) (a) and (180°, 270°) (b).*

Lastly, to establishing the optimal flow control coefficient applied to either preferential azimuthal orientation (θ = 90° or 270°), coupled to the targeted forebody orientation ϕ that results in either a negative or a positive side force, the flow control parameter is varied over a range of $C_\mu/C_{\mu,max}$ and the changes in the forces are recorded. The resulting changes in the force coefficients are shown for the negative and positive base side force in Figures 8a and b, respectively. As the flow control at θ = 90° (Figure 8a) is designed to counter a negative side force, it facilitates a net increase in C_S. Conversely, the flow control applied at θ = 270° (Figure 8b) is designed to counter a positive side force of the base flow and thus generates a net decrease in C_S. Common to both cases, it is shown that effectiveness of the flow control is facilitated at rather low levels of C_μ. Moreover, there is a rather sharp increase in the induced change in C_S within a narrow range of C_μ. Past this transition there is a saturation level in the achieved ΔC_S with further increase in C_μ. This points to an optimum level of the flow control parameter that achieves the maximum effect. It should be pointed out that although the current study deploys only a single actuator for the research purposes, any application would utilize an actuator on either side, such that the bi-directional change in side forces can be attained on command, without a need for the actuator azimuthal adjustments.

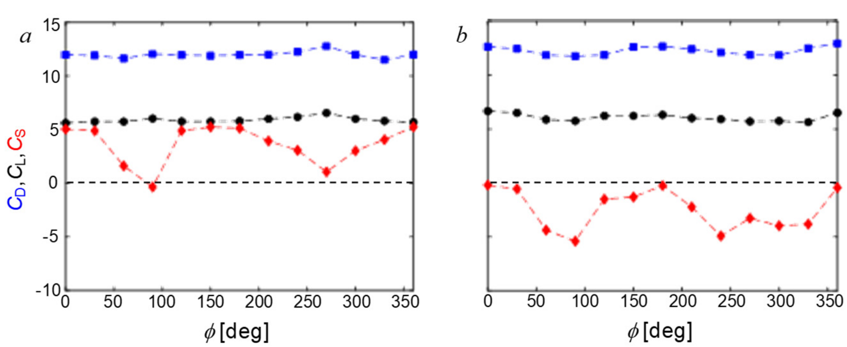

Figure 9. *Force coefficients C_D (■), C_L (●), and C_S (♦) with the forebody azimuthal orientation ϕ (a), and the flow controlled by the jet at θ = 90° (a) and 270° (b) for the model at α = 60° (Re_D = 7.9·10^4).*

The present concept of flow control of the aerodynamic loads relies on an indirect control of the dominant vortices that are the primary source of the non-zero net side force (and the yawing moment). The flow control primarily affects the separating flow at the juncture between the forebody and the cylindrical body. The effect of the actuation was first investigated by exploring the aerodynamic loads in Figure 6. Here, the effectiveness of the control jet is assessed over a full range of the azimuthal orientations of the forebody. To address the two characteristic base flow realizations, when the induced net side force is either negative or positive, the flow control jet is preset at either θ = 90° or 270°. When the synthetic jet actuator was set at an azimuthal angle of θ = 90° (i.e., pointing to the right in an upstream view) and the ogive forebody was rotated as in Figure 5a (for α = 60°, Re_D = 7.9·10^4), the (unknown) surface perturbations are essentially varying such to alter the symmetry of the forebody vortex pair relative to the azimuthal orientation of the actuation jet. Figure 9a shows the three resulting global aerodynamic force coefficients at the same azimuthal position relative to the ogive forebody and cylinder as in the absence of actuation (Figure 5a). These data show that the actuation significantly alters the magnitude and direction of the induced side forces within the domains centered about $\phi = 90°$ and $270°$ while rendering the effect on the side forces throughout the rest of the azimuthal domain positive but of a much smaller magnitude. The presence of the actuation in these domains of the high effectiveness *reverses* the direction of each of the side forces that would otherwise be induced at $\phi = 90°$ and $270°$ and alters its sign, therefore implying a change and reversal in the vortical asymmetry. Overall, actuation by the control jet kept at $\phi = 90°$ results in the net positive side force, regardless of the forebody orientation. As it could be expected based on the duality of the effects shown in Figure 8, the opposite arrangement, where the synthetic jet is fixed on the opposite side ($\theta = 270°$) induces exactly the opposite effect to the studied jet orientation at $\theta = 90°$ (Figure 9a). The mirrored jet predominantly affect the opposing sense of the vortical asymmetry, thereby significantly opposing the positive side forces, in a similar manner that the jet

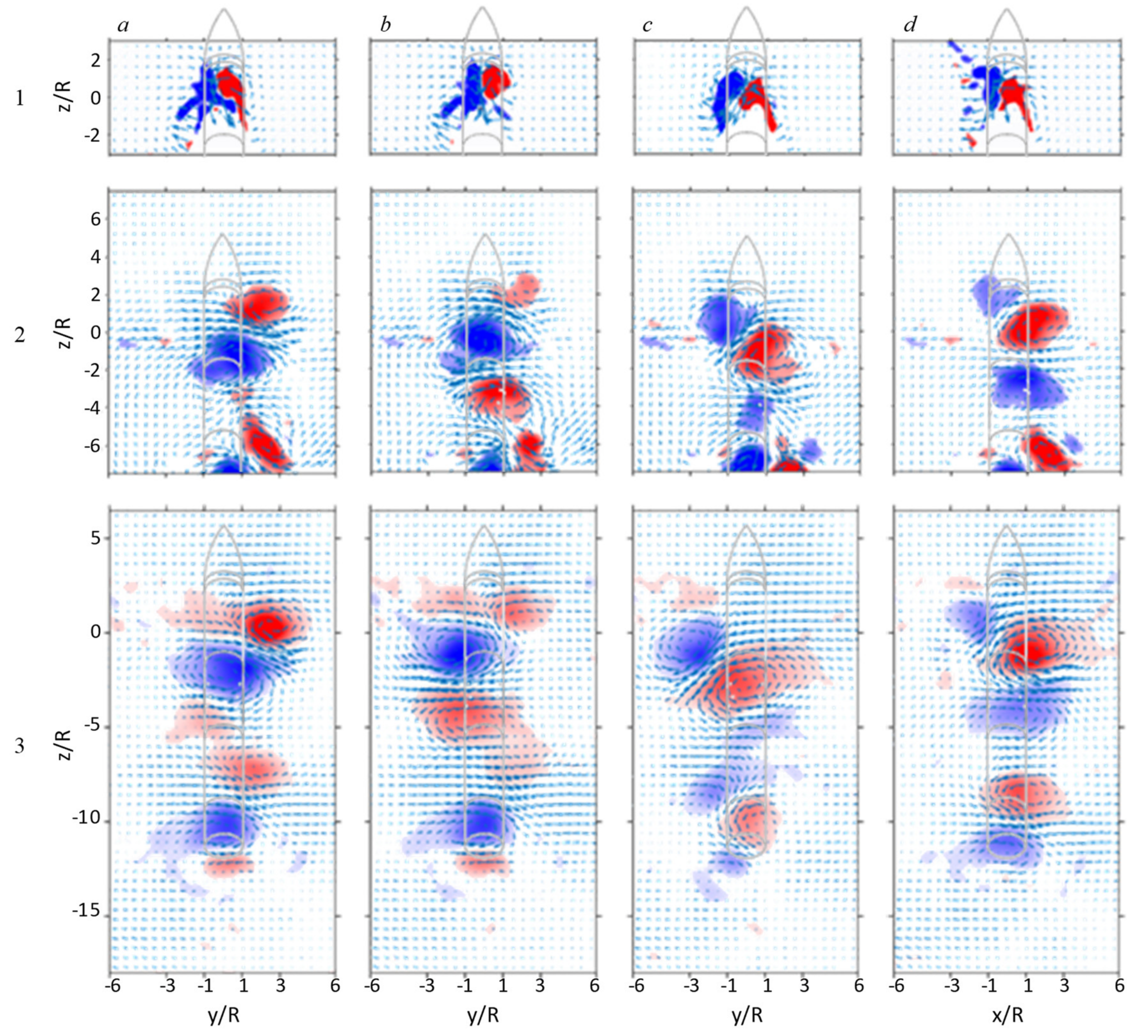

Figure 10. *Raster contour plots of the mean streamwise vorticity with in-plane mean velocity vectors measured at x/D = 2 (row 1), 5 (row 2), and 9 (row 3) for the base flow ($\alpha = 60°$, $Re_D = 1.14 \cdot 10^5$) at forebody orientation $\phi = 90°$ (column a) and controlled at $\theta = 90°$ (column b), and for the base flow at $\phi = 180°$ (column c) and controlled at $\theta = 270°$ (column d). Vorticity contour levels are the same as in Figure 5.*

at $\theta = 90^o$ is shown to affect the azimuthal subdomains that induce negative side forces. Therefore, regardless of the forebody orientation, actuation by the jet at $\theta = 270^o$ always induces a negative side force, as seen in Figure 9b. It is therefore inferred, as already proposed during the discussion of Figure 8, that integration of the two jets, at $\theta = 90^o$ and 270^o would be sufficient for control of either vortical asymmetries. Also, if the objective would be to maintain the side force close to zero, some tuning of the control jet parameter would be done, as the present results indicate the "overshooting" of the suppression effect and induction of the side force of the opposite sign.

The main features of the wake flow past a slender body at high angle of incidence were already discussed in connection with Figure 4. In order to gain insight into the changes in the flow structure that is associated with each of the opposite side forces that act on the body by each of the control scenarios depicted in Figure 9, sPIV measurements are acquired at three streamwise cross stream planes at $x/D = 2$, 5, and 9 for inclination angle of $\alpha = 60°$. The resulting flow fields are shown in Figure 10 along with overlaid silhouettes of the projected body. Figure 10 includes two pairs of columns (a, b) and (c, d) for forebody orientations $\phi = 90°$ and 270^o, respectively. The columns in each pair corresponds to the base flow (a and c) and the flow in the presence of actuation when the actuator is placed azimuthally at $\theta = 90°$ and 270° (b and d, respectively). Rows 1, 2, and 3 correspond to $x/D = 2$, 5, and 9, respectively. Figures 10.1a and c and 10.1b and d show the effect of the actuation on the forebody vortices. As can be seen, the two pairs of streamwise vortices become detached from the surface unevenly and evolve into the asymmetric and tilted pairs, and this effect is accentuated by the actuation where the CW vortex in Figures 10.1a and b and the CCW vortex in Figures 10.1c and d begins to turn over the opposite sense vortex. This effects becomes more pronounced in Figures 10.2a and c. Figures 10.2a, b, c, and d show that in addition to the forebody vortices there are additional streamwise vortices that are formed by flow separation off the leeward side of the cylindrical body. In the absence of actuation (Figures 10.2a and c) the secondary, somewhat weaker (wake) vortices become aligned by the induced flow of the forebody vortices in a nearly columnar array of counter-rotating vortices. In the presence of actuation, the leading forebody streamwise vortex (CW and CCW in Figures 10.2a and 10.2c, respectively) become significantly diffused and weaker (Figures 10.2b and 10.2d), while its pair vortex of the opposite sense (CCW and CW, respectively) in the column gains in circulation. The induced flow by the intensified CCW (in Figure 10.2b) and CW (in Figure 10.2d) vortices acts to pull and intensify the next opposite sense vortex (below) into the column. As shown in Figures 10.3a and 10.3c, the column of alternating streamwise vortices also forms in the absence of the actuation but it is primarily affected by the dominant forebody vortex in the surface proximity (CW in Figures 10.2a and 10.3a and CCW in Figures 10.2c and 10.3c). *However, remarkably, the weakening of the leading vortex by the actuation in Figures 10.2b and 10.2d leads to effective altered order of the vortex stack in Figures 10.3b and 10.3d.*

V. Control of the Body Dynamic Coupling to the Wake

As noted in discussion of Figure 5a, coupling to the induced vortices at high angles of attack may lead to the body unstable response. Up to this point, only the stable body responses were considered. To survey the possible unstable responses, a continuous pitch up/down maneuver is executed first. During these tests, the slender model ($L/D = 11$) is commanded to steadily pitch up from $\alpha = 45°$ to 60° followed by the pitch down back to 45°. The pitch rates are varied over an order of magnitude, ranging from 0.1 – 1 deg/s. Although the details of particular onsets and terminations of the model instability somewhat change with the changing pitching rate, two scenarios emerged as characteristic for the unsteady body response. In an unsteady-response scenario, depending on the forebody

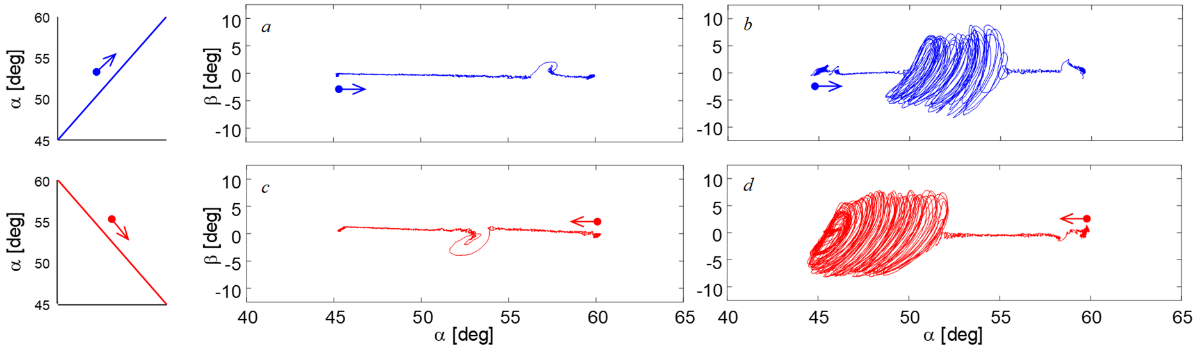

Figure 11. *Yaw angle variation during the increasing (a,b) and decreasing (c,d) pitch sweep 45 ° < α < 60 ° for the forebody azimuthal orientation ϕ = 0 ° (a,c) and 30 ° (b,d).*

azimuthal orientation ϕ, the body trajectory may either be initially displaced in yaw but subsequently recovered (Figures 11a and c), or the body can undergo instability in yaw (and roll), as shown in Figures 11b and d. The other notable feature is that there is a hysteresis in the onsets and terminations of instability depending on the pitching direction. This is attributed to the different starting flow states. When pitching up from α = 45°, the body wake is still dominated by the forebody vortices, which peel off of the surface closer to the forebody with the increase in the pitching angle, giving a way to a more prominent role of the cylinder body wake. When pitching down, the starting wake at α = 60° is in a complex state of the interacting cylinder body shear layers and forebody vortices, and it would intuitively take longer for such a wake to recover its corresponding more regularized state (established during the pitch-up motion). It is argued that this is the main reason for the observed hysteresis, as both the onset and termination of instability are delayed relative to their counterparts during the pitch-up motion. There does not seem to be any notable difference in terms of the amplitude of oscillations during the instability, as in both the pitch up and down, recorded oscillations in yaw were about β = ±5°.

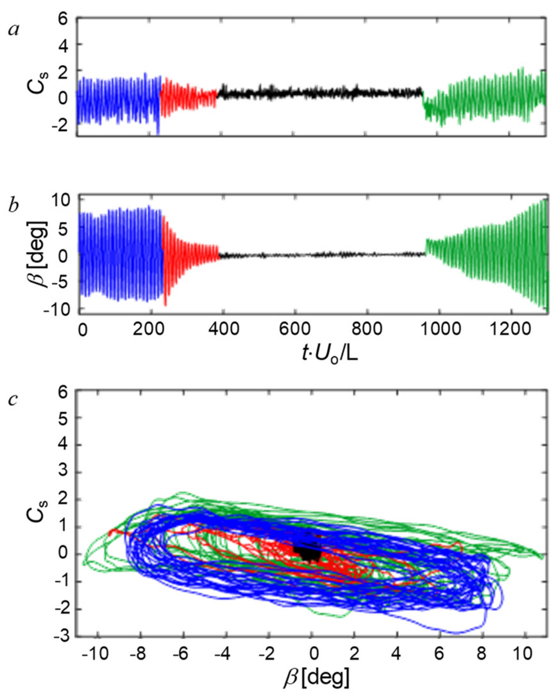

Figure 12. *Time evolution (a, b) and phase relationship (c) of the side force coefficient C_S and the yaw angle β for the l/D = 2 forebody model at α = 50°. Effect of aerodynamic model stabilization by the jet actuation is shown between 232 < $t{\cdot}U_o/L$ < 961.*

The present investigations demonstrated that within the narrow ranges of angles of incidence (50° < α < 60°) the coupling between the forebody vortices and the cylinder's near-wake can lead to base flow instabilities of the wire-supported model that is manifested by significant pitch and yaw oscillations. Although such instabilities may not be directly detectable on sting-mounted model, the investigations of Zilliac et al. (1991) indicate their presence as the azimuthal position of forebody is adjusted at $\alpha \sim 60°$. These observations clearly posed the question as to whether manipulation of forebody vortices and therefore their interaction with the cylinder's wake vortices can be used to stabilize or destabilize the model when it is naturally unstable or stable within this incidence range.

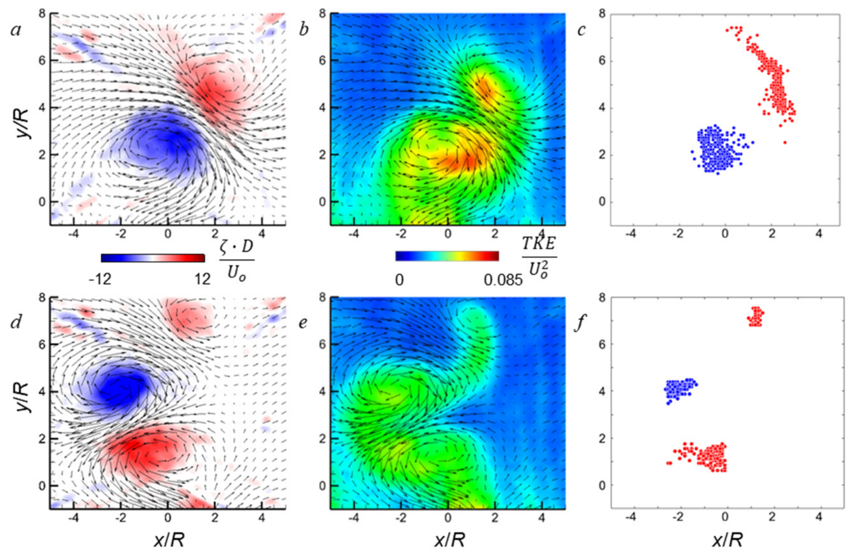

Figure 13. *Contour plots of the POD-reconstructed time-averaged vorticity (a, d) and turbulent kinetic energy (b, e) fields at x/D = 8, along with the planar distributions of the vortex cores (c, f) for the unstable (a– c) and stabilized (d–f) model dynamics of Fig. 12.*

The present investigation showed that when the azimuthal position of the ogive forebody was set to $\phi = 60^{\circ}$, the model exhibits significant time-periodic oscillations in incidence and yaw (±6°) at incidence of $\alpha = 50^{\circ}$. As noted in connection with Figure 5, when the model is stable in the absence of actuation (e.g., at $\alpha = 60^{\circ}$), $C_S < 0$ and the major axis of the forebody vortex pair is slanted to the left (cf. Figure 5). Simultaneously-measured time traces of $C_S(t)$ and $\beta(t)$ in Figures 12a and b for $0 < t^+ < 232$, ($t^+ = tU_o/L$) show that C_S oscillates between -2.9 and 1.82 (the nominal mean is about -0.34) with a characteristic frequency of about 7 Hz ($St_L = 0.0093$). Based on the results of Section IV, the azimuthal position of the jet relative to the forebody is selected such that it if the model was stable, it would reverse the symmetry of the forebody vortices ($\theta = 90^{\circ}$), and result in an increase in the side force. When jet actuation is activated at $t^+ = 232$ through 961, and the traces of $C_S(t)$ and $\beta(t)$ (Figures 12a and b) exhibit a strong decay in oscillations over a characteristic time $\Delta t^+ = 157$ (about 16 oscillations periods), and the peak-to-peak oscillations of C_S and β are attenuated by factors of three and five, respectively. While the yaw angle effectively becomes zero, the side force varies slightly around a mean level of +0.26, indicating that the jet actuation level could be adjusted so that the effected mean side force vanishes. The time-dependent traces show that when the jet actuation is terminated at $t^+ = 961$, there is a clear commensurate jump in the magnitudes of both C_S and β. The unsteady baseline oscillations resume with slowly-increasing magnitude while the oscillations commence about a negative “offset” in C_S which is first negative and then gradually increases. It is noteworthy that the rate of increase in the amplitude of β is slower than in C_S apparently as a result of the model’s inertia. However, it does not appear that the model fully returns to its original motion before the onset of actuation. This is further accentuated by the C_S-β phase plot in Figure 12c, where the trajectory at the end of the model’s response appears offset from the initial limit cycle. It is also noted that the relatively long transitions associated with the onset and termination of the actuation might be associated with the gradual coupling (or decoupling) between the forebody vortices and the vortical structures in the wake of the cylinder.

Color raster plots of the streamwise vorticity downstream of the model (cf., Figure 5) indicate that the actuation effects significant changes in the vortex topology (Figures 13a and d, respectively). The unstable model is characterized by the formation of a vortex pair whose major axis is slanted to the right, and it is remarkable that although the model undergoes unsteady oscillations, the time-averaged vorticity distributions indicate that the coherence of the vortex pair is largely preserved although the time-averaged CCW vortex appears weaker and its streamwise vorticity is less

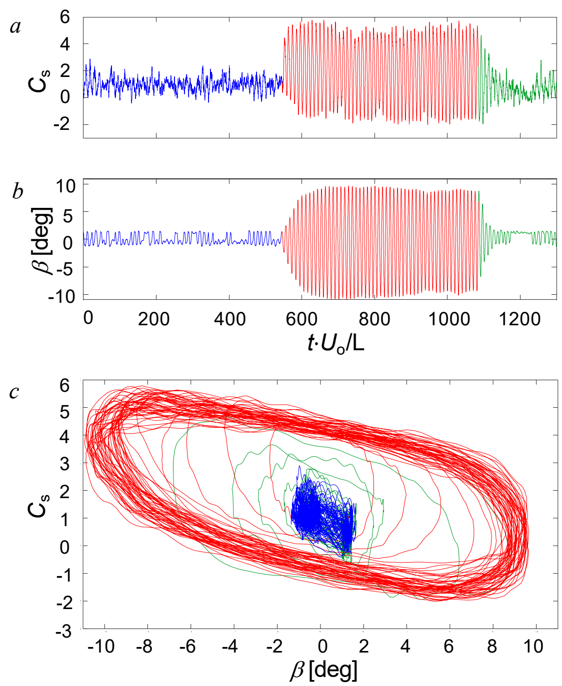

Figure 14. *Time evolution (a, b) and phase relationship (c) of the side force coefficient C_S and the yaw angle β for the l/D = 2 forebody model at $\alpha = 55°$. Effect of aerodynamic model destabilization by the jet actuation is shown between $545 < t \cdot U_o/L < 1085$.*

concentrated than in the opposite CW vortex. Following the onset of actuation that leads to model stabilization, the symmetry of the forebody vortex pair is flipped horizontally, and the vorticity map indicates that the cores of the CW and CCW vortices have similar distributions and strength. This map also shows the appearance of an additional CCW vortex near the upper edge of the field of view that might be associated with the presence of the jet actuation. The corresponding concentrations of turbulent kinetic energy (TKE) within this view (Figures 13b and e) show that compared to the stabilized flow, in the unstable flow in the absence of actuation the TKE is somewhat more spread and is higher near the centers of the vortex cores suggesting evidence of some oscillations. This effect is also apparent in the map that depicts the centers of the vortex cores in instantaneous realizations based on equivalent Γ_1 vortex detection scheme on the POD-reconstructed flow field. In concert with the vorticity concentrations in Figure 13a, the cores of the CCW vortices are indeed spread while the cores of the CW vortices appear clustered. In the presence of actuation, the clustering of the cores is even more pronounced.

The receptivity of the model to unstable oscillations within this range of incidence was also explored by using the actuation to destabilize the model when the base flow is nearly-stable. When the azimuthal position of the ogive forebody was set to $\phi = 0°$, the model appeared to be stable at $\alpha = 55°$ with relatively low-level time-varying oscillations in $C_S(t)$ and $\beta(t)$ with both the average means and amplitudes of about 1 (C_S) and about zero and 1.5° (β) (Figures 14a and b) prior to the onset of actuation at $t^+ = 545$. The corresponding C_S-β a phase plot (Figure 14c) is clustered about (0°,1) and is nearly featureless. The actuation jet which is placed at $\theta = 90°$ is activated at $t+ = 545$, and results in strong oscillations of the C_S at frequency of about 7 Hz ($St_L = 0.0093$), which is about the same as the characteristic frequency of natural body oscillations (Figure 12) that seem to amplify very rapidly to a nominal an amplitude of 3.9 by comparison to the corresponding oscillations of the yaw angle that reach an amplitude of 10.3 within nine cycles following the onset of the actuation as the body motion couples to the change in the force. It is noteworthy that following the actuation, the slightly positive C_S becomes almost instantly biased towards high magnitude sides force of the same sign, and the oscillating force remains offset. By comparison to the return of the model to the unstable state in Figures 14a and b, the amplification here is significantly higher. When the actuation is turned off at $t+ = 1085$, both C_S and β exhibit transitional decaying response that is somewhat longer for C_S. The phase plot in Figure 14c shows the return to base state from the limit cycle of the unstable state.

Similar to the changes associated with stabilization in Figures 13, the changes in the flow field that are associated with the destabilization are shown in Figure 15. The time-averaged color raster plots

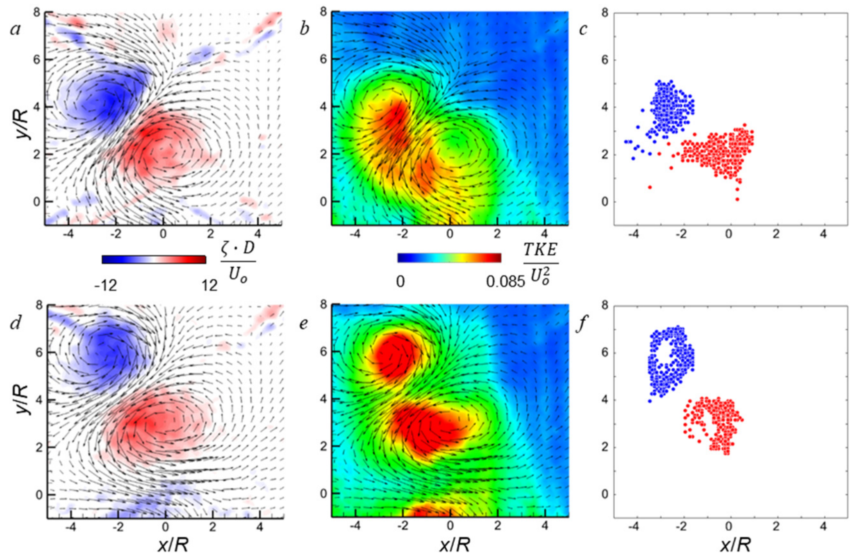

Figure 15. Contour plots of the POD-reconstructed time-averaged vorticity (a, d) and turbulent kinetic energy (b, e) fields at x/D = 8, along with the planar distributions of the vortex cores (c, f) for the stable (a– c) and destabilized (d–f) model dynamics of Fig. 14.

of the streamwise vorticity concentrations (Figures 15a and d) capture a distinct asymmetric vortex pair with its major axis tilted to the left. It is remarkable that the symmetry of this vortex pair does not change when the model becomes unstable in the presence of actuation (Figure 15d) although both vortices are somewhat displaced upward and remain coherent. Because these data do not suggest significant coupling between the vortex pair and the stability of the body, it is conjectured that the unstable motion is triggered by coupling of the jet actuation to the wake of the cylinder rather than to the forebody. Some differences are noted, though, when examining the distributions of the turbulent kinetic energy for these two flow fields (Figures 15b and e). These data show that during when the model is stable (Figure 15b), the peak turbulent kinetic energy is measured in the interaction zone in between the two vortices. However, the turbulent kinetic energy levels generally increase when the model is unstable and the vortices appears to be farther separated. The cores of the instantaneous vortices (using vortex detection based on the Γ_1 criterion, Figures 15c and f) show distinct orbits of the vortex cores when the model is unstable indicating precession about the central position of their trajectory.

VI. Conclusions

The present experimental investigations explore tailored modification of the aerodynamic loads on a slender axisymmetric body at high incidence by exploiting the dominant streamwise vortical structures using aerodynamic flow control approach. Although the most prior work considered the direct control of the forebody vortex pair by placing the flow control elements in the vicinity of their origin, the present effort focuses rather on the direct control of the separating flow on the leeward body side, which significance rises with the increasing incidence. In turn, the directly controlled wake alters the dominant vortical composition through its inherent coupling. Therefore, the present flow control approach affects the dominant streamwise vortices, and consequently the aerodynamic loads, in an indirect fashion.

This study considers the flow over a slender axisymmetric cylinder model (L/D = 11), including the tangent ogive forebody of the length l/D =2. The investigations are focused on control of autonomously-formed, successively shed, pairs of forebody vortices over a range of angles of inclination (25° < α < 65°), with the emphasis placed on the high range of angles 45° < α < 60°. A single azimuthally-adjustable flow control module is integrated into the cylindrical body, just downstream from the forebody. The jet module incorporates a synthetic jet having a single azimuthal orifice measuring 0.6 × 15.7 mm.

As the resulting wake vortical composition is sensitive to the forebody azimuthal orientation, two characteristic scenarios are considered, resulting in the preferential orientation of the streamwise vortices that consequently induce a net non-zero side force of different signs. It is shown that there is a range of the azimuthal orientations of the flow control jet for which its effect counters the naturally-induced side force. Moreover, the flow control in either of the two characteristic base flow scenarios can effect a single-sign side force regardless of the forebody orientation. The flow field sPIV measurements revealed the mechanism of the flow control alteration of the 'stacked' vortical composition of the flow. Upon activation, the flow control, through the wake, diffuses and weakens one of the primary forebody vortices. In turn, its pair that remains in closer proximity to the body successively induces the opposing-sense vortex, forming the alternate dominant vortex pair. Thereby, the wake's vortex 'stack' remains composed of the alternating CW and CCW vortices that successively and cooperatively interact, only the dominant top vortex pair (closest to the body and consequently of the most influence of the body loads) switch from CW-CCW to CCW-CW, or vice versa.

Finally, the unique non-sting body support allows for the body to couple to the changing aerodynamic loads, and it is shown that there are instances in which the body can undergo unstable motions, predominantly in yaw (relative to its own coordinate system). It is demonstrated that the same flow control approach that imparts incremental changes in the realized side force on the stable body can be utilized for stabilizing the naturally unstable body coupling to the wake, or even for triggering the body unstable response from its otherwise stable state. It is argued that the bi-directional side force control can be achieved by integration of two independent synthetic jet actuators, where each of them would impart a single-sense side force offset.

Acknowledgment
This work was supported by the Army Research Office (monitored by Dr. M. Munson).

References
Almosnino, D. and Rom, J., "Lateral Forces on a Slender Body and Their Alleviation at High Incidences", J. Spacecraft and Rockets, **5**, 1981.

Chapman, G.T, Keener, E.R, and Malcolm, G.N, "Asymmetric Aerodynamic Forces on Aircraft Forebodies at High Angles of Attack - Some Design Guides," AGARD Conference Proceedings AGARD-CP-199 (12), 1976.

Deng, X., Wang, G., Chen, X., Wang, Y., Liu, P. and Xi, Z., "A Physical Model of Asymmetric Vortices Flow Structure in Regular State over Slender Body at High Angle of Attack," *Sci. China E: Technological Sciences*, **46**, 2003.

DeSpirito, J., "CFD Aerodynamic Characterization of 155-mm Projectile at High Angles-of-Attack," AIAA Paper 2017-3397, 2017.

Fagley, C., Farnsworth, J., Seidel, J. and McLaughlin, T., "Experimental Study of Open Loop Plasma Actuation on a von Kármán Ogive," AIAA Paper 2012-0905, January 2012.

Hoerner, S.F. and Borst, H. V. "Fluid-Dynamic Lift," 2nd Edition, Published by L. A. Hoerner, 1985.

Kalyankar, H., Taubert, L. and Wygnanski, I., "Re-orienting the Turbulent Flow over an Inclined Cylinder of Finite Aspect Ratio," AIAA Paper 2018-4026, June 2018.

Keener, E. and Chapman, G., "Onset of Aerodynamic Side Forces at Zero Sideslip on Symmetric Forebodies at High Angles of Attack," AIAA Paper 74-0770, 1974.

Lambert, T.J., Vukasinovic, B., and Glezer, A., “A Six Degrees of Freedom Dynamic Wire-Driven Traverse,” *Aerospace,* **3**:11, 2016.

Lambert, T. J., Vukasinovic, B., and Glezer, A. “Aerodynamic Flow Control of Axisymmetric Bluff Body by Coupled Wake Interactions,” *AIAA J.* **56**, pp. 2992-3007, 2018.

Leu, T.-S., Chang, J.-R. and Lu, P.-J., “Experimental Investigation of Side Force Control on Cone-Cylinder Slender Bodies with Flexible Micro Balloon Actuators,” *Exp. Ther. Fl. Sci.*, **29**, 2005.

Ma, B.-F. and Liu, T.-X., “Low-Frequency Vortex Oscillation around Slender Bodies at High Angles-of-Attack,” *Phys. Fluids,* **26**, 2014.

Mahadevan, S., Rodriguez,J. and Kumar, K., “Effect of Controlled Imperfections on the Vortex Asymmetry of a Conical Body,” *AIAA J.* **56**, pp. 3460-3477, 2018.

Nelson, R. and Fleeman, E., “High Angle-of-Attack Aerodynamics on a Slender Body with a Jet Plume,” *J. Spacecraft,* **12**, 1975.

Porter, C., Fagley, C., Farnsworth, J., Seidel, J. and McLaughlin, T., “Closed-Loop Flow Control of a Forebody at a High Incidence Angle,” *AIAA J.*, **52**, 2014.

Rao, D., Moskovitz, C. and Murri, D., “Forebody Vortex Management for Yaw Control at High Angles of Attack,” *J. Aircraft*, **24**, No. 4, pp. 248-254, April 1987.

Sato, A., Nishida, H. and Nonaka, S., “Preliminary Study on Aerodynamic Control of High-Angle-of-Attack Slender Body using Blowing from Penetrating Flow Channels,” *Int. J. Aero Eng*, 1602043, 2016.

Schnepf, C. and Schülein, E., “Numerical Study on the Impact of a Maneuver on the Phantom-Yaw-Effect in Transonic Flow,” AIAA Paper 2018-4124, June 2018.

Seidel, Jürgen, and Thomas Mclaughlin, “Feedback Flow Control: A Heuristic Approach.” *AIAA Journal*, arc.aiaa.org/doi/10.2514/1. J056884. 29 June 2018.

Skow, A., Moore, W. and Lorincz, D., “Control of Forebody Vortex Orientation to Enhance Departure Recovery of Fighter Aircraft,” *J. Aircraft*, **19**, 1982.

Stucke, R., “High Angle-of-Attack Yaw Control using Strakes on Blunt-Nose Bodies,” Ph.D. Dissertation, Univ. of Toledo, December 2006.

Thomson, K.D. and Morrison, D.F. “The Spacing, Position and Strength of Vortices in the Wake of Slender Cylindrical Bodies at Large Incidence,” *J. Fluid Mech*, **60**, 1971.

Ward, K. and Katz, J., “Development of Flow Structures in the Lee of an Inclined Body of Revolution”, *J. Aircraft*, **26**, 1989.

Ward, K. and Katz, J., “Topology of the Flow Structures Behind an Inclined Projectile: Part A”, *J. Aircraft*, **26**, 1989.

Ward, K. and Katz, J., “Topology of the Flow Structures Behind an Inclined Projectile: Part B”, *J. Aircraft*, **26**, 1989.

Williams, D., El-Khabiry, S. and Papazian, H., "Control of Asymmetric Vortices Around a Cone-Cylinder Geometry with Unsteady Base Bleed," AIAA Paper 89-1004, March 1989.

Williams, D. and Papazian, H., "Forebody Vortex Control with the Unsteady Bleed Technique," *AIAA J.*, **29**, 1991.

Wu, G., Wang, T. and Tian, S., “Investigation of Vortex Patterns on Slender Bodies at High Angles of Attack,” *J. Aircraft,* **23**, 1986.

Yanta, W. and Wardlaw, A., “Laser Doppler Velocimeter Measurements of Leeward Flowfields on Slender Bodies at Large Angle-of-Attack,” AIAA Paper 77-0668, June 1977.

Yanta, W. and Wardlaw, A., “Flowfield about and Forces on Slender Bodies at High Angles of Attack,” *AIAA J.*, **19**, 1981.

Yanta, W. and Wardlaw, A., “The Secondary Separation Region on a Body at High Angles of Attack,” AIAA Paper 82-0343, January 1982.

Zilliac, G., Degani, D. and Tobak, M., “Asymmetric Vortices on a Slender Body of Revolution,” *AIAA J.*, **29**, May 1991.